Effects of different stratification changes on both sides of the typhoon track on near-inertial energy propagation

XingShang Qian[1,3], GuangHong Liao[1,2*], Lei Zhou[3], Juncheng Xie[4]

[1]Key Laboratory of Marine Hazards Forecasting, Ministry of Natural Resources, Hohai University, Nanjing, 210098, China

[2]Laboratory for Regional Oceanography and Numerical Modeling, Pilot National Laboratory for Marine Science and Technology, Qingdao, 266000, China

[3]School of Oceanography, Shanghai Jiao Tong University, Shanghai, 200030, China

[4]Marine Science and Technology College, Zhejiang Ocean University, Zhoushan, 316022 China

Corresponding Author: GuangHong Liao (Email: liaogh@hhu.edu.cn)

Key Points:

- "Heat pumping" and "cold suction" of typhoons changes the ocean stratification
- Enhanced ocean stratification condition accelerates the propagation of near-inertial waves into the ocean interior.
- NIE injection to the deep ocean from the left side of typhoon is stronger although the wind energy input is weaker than the right side

Abstract

Near-inertial waves (NIWs) originate in the ocean upper mixed layer. When they have a large horizontal scale, which is characteristic of an atmospheric storm, they are difficult to propagate vertically below the mixed layer. The β-effect and the mesoscale vorticity are considered as two important mechanisms for guiding the downward propagation of near-inertial energy (NIE). In this paper, the effects of "heat pumping" and "cold suction" of typhoons on the ocean stratification are analyzed. It is found that changes in stratification enhance the vertical propagation of NIWs from the mixed layer into the ocean interior on the left side of the typhoon track. To illustrate the impact of stratification changes on both sides of typhoon tracks, the Regional Ocean Modelling System (ROMS) is used to simulate the NIWs generated by Typhoon Kalmaegi in 2014. The results show that, although the wind energy input on the right side of the typhoon track is higher than that on the left side, the NIE injection to the deep ocean from the left side is stronger due to the different dissipation and stratification responses. Our work improves the understanding of the generation, propagation, and dissipation mechanisms of NIWs during typhoons.

Plain Language Summary

Near-inertial waves (NIWs), as a ubiquitous spectral peak in moored current-meter data, comprise half of the energy and most of the vertical shear in the ocean internal wave spectrum, and they are thought to be major drivers of upper-ocean mixing. NIWs mainly originate in the ocean upper mixed layer, with a large horizontal scale which is characteristic of an atmospheric storm, they are difficult to propagate vertically below the mixed layer. In previous studies, the β-effect and the mesoscale vorticity are considered as two important mechanisms for guiding the downward propagation of near-inertial energy (NIE). In this work, the effects of "heat pumping" and "cold suction" of typhoons on the ocean stratification are analyzed based on observation and numerical model. It is found that changes in stratification enhance the vertical propagation of NIWs from the mixed layer into the ocean interior. Although the wind energy input on the right side of the typhoon track is higher than that on the left side, the NIE injection to the deep ocean from the left side is stronger due to the different dissipation and stratification responses. Our work improves the understanding of penetration of wind-generated NIWs into the ocean interior.

1 Introduction

The ocean is like a field of harmonic oscillators, which resonantly amplify forcing at local inertial frequency *f*. In the upper ocean the near-inertial peak contains about half the kinetic energy in the internal wave spectrum (Ferrari and Wunsch, 2009) and similarly a large fraction of shear (Alford et al., 2016). Near-inertial waves (NIWs) are a significant energy source in driving the diapycnal mixing in the ocean, for maintaining strength of the Meridional Overturning Circulation (Munk and Wunsch, 1998). Wind forcing is a major energy source for NIWs, with an estimated about 0.47 TW of wind energy converted to surface near-inertial motion per year (Alford, 2003). Typhoons are among the wind events capable of exciting strong NIWs, because of their appropriate sizes and strong wind stress, thereby inputting mechanical energy into the near-inertial band (Pollard 1970; Price 1981; Shay and Elsberry 1987; Shay et al., 1990; Cuypers et al., 2013; Alford et al., 2016). NIWs energy radiates into the upper thermocline with an e-folding time scale similar to an inertial period. In the thermocline, wave propagation is substantially modified by the background environment including ocean currents and stratification.

Typhoons are known to impact oceanic stratification in two aspects (Chen et al., 2013; Zhou et al., 2019). The first mechanism is referred to as “heat pumping”. When a typhoon passes over a region, the strong wind stress with typhoon causes intense mixing and entrainment, leading to the cooling of the sea surface, deepening the mixed layer, and warming the subsurface (Jacob et al., 2000; Price, 1981, 1983, 1994; Sanford et al., 2011; Yang et al., 2015). The “heat pumping” is much stronger on the right side of a typhoon track, as there is larger wind stress and the same direction of rotation (Price, 1981; Chang and Anthes, 1978). The second effect is known as “cold suction”. Wind stress generated by typhoon causes the uplift of isopycnal due to the Ekman suction. Such process cools the subsurface and counteracts the warm anomaly caused by the "heat pumping" in the subsurface, altering the energy input of typhoons to the ocean and its global impact (Zhou et al., 2019). For a long time, the “heat pumping” was known to be the dominant mechanism for the thermal response of the sea surface and subsurface (Emanuel 1986, 2001; Korty et al., 2008; Pasquero and

Emanuel, 2008; Sriver and Huber 2007; Zhang et al., 2016). However, recent studies have revealed that the “cold suction” also plays a crucial role in the subsurface for relatively weak typhoons (Park, et al., 2011). Field observations of Typhoon Kalmaegi were made via a cross-shaped array of buoys and moorings in the northern South China Sea (SCS). In-situ data revealed cold anomalies in the mixed layer at each station following Typhoon Kalmaegi’s passage. Furthermore, warm anomalies were observed in the subsurface on the right side of the typhoon track, while cold anomalies were dominated on the left side. These suggest that the “cold suction” effect has a more significant influence on the stratification of the left side of the typhoon track (Zhang et al., 2016).

Typhoon processes significantly alter the dynamics and thermohaline environment of the ocean. Previous studies have investigated the effect of different stratification changes on both sides of a typhoon track as the thermal response (Zhang et al., 2016, 2018). However, the analysis of different effects of “heat pumping” and “cold suction” on the stratification and the resulting dynamical responses is still lacking. While more than 50% of the wind work input to the near-inertial frequency band is dissipated in the upper ocean (Furuichi et al., 2008; Zhai et al., 2009), some studies have shown that the NIWs generated by typhoons propagate faster and longer, even reaching depths of 1000 m (Price, 1983; Hou et al., 2022; Cuypers et al., 2013; Ma et al., 2022). Additionally, since climate models cannot yet directly resolve small scale processes like NIWs, it is necessary to parameterize their effects in models. The existing parameterization schemes may be inaccurate without considering of the effect of typhoon-induced stratification changes on the propagation of near-inertial energy (NIE) (Zhou et al., 2019). Unfortunately, our understanding of the ocean’s dynamic responses to typhoons is still lacking due to scarce in-situ observations.

NIWs originate wind events with a length scales characteristic (1000 km) of the atmospheric forcing (Pollard, 1980; D’Asaro et al., 1995). One difficulty with this scenario is that these waves hardly propagate vertically below the mixed layer. An NIW with a horizontal length scale of 1000 km can remain in the mixed layer for longer than one year (Gill, 1984; Asselin and Young, 2020). Ocean Storms

Experiment shows that the β-effect results in a steady increase of the north-south wavenumber of the NIW with time (D'Asaro et al., 1995). On the other hand, the mesoscale vorticity also has long been hypothesized to cause local frequency shifts analogous to the β-effect (Kunze, 1985). The vertical group velocity of near-inertial waves is $C_g \approx -N^2 k_h^2 / 2 f k_z^3$, with N the buoyancy frequency, f the Coriolis frequency, k_{h} the horizotnal wavenumber, and k_{z} the vertical wavenumber. the steady increase in horizontal wavenumber accelerates the vertical propagation. A theory proposed by Young and Ben Jelloul (1997) also supports that the mesoscale eddy accelerates the downward propagation of NIWs. However, the ocean stratification is assumed unchanged in all these works, which may lead to bias in group velocity estimates.

In the study, the Regional Ocean Modelling System (ROMS) combined the field observation data is used to investigate the effect of different stratification changes on NIWs propagation. The paper is organized as follows: Section 2 introduces the data and model configuration used in this work. Section 3 analyzes the results, especially focusing on the different stratification impacts and the associated differences in the NIE on both sides of the typhoon track. The final section provides conclusions and discussions.

2 Data and Model

2.1 In-situ data

The observational data utilized in this study was collected from a network of 5 buoys and 4 moorings deployed in the South China Sea (SCS) and consisted of measurements such as Acoustic Doppler Current Profilers (ADCP), Conductivity-Temperature-Depth (CTD) sensors, and Seaguard oceanic current instruments. Detailed information regarding the observations can be found in Zhang et al., (2016, 2018). The locations of the buoys and moorings used for data collection are indicated by red dots in Figure 1. To ensure the completeness of data, we fills in missing values using the linear interpolation for time series data at each depth.

2.2 Best-track Typhoon Data

Tropical cyclone (Kalmaegi) generated in northwest Pacific intensified to the typhoon level at 12:00 UTC on September 13, 2014, then entered the SCS around 15:00 UTC on the same day, and finally made landfall in Wenchang, Hainan Province, China at 03:00 UTC on September 16, 2014. The Best-track data for Typhoon Kalmaegi used in this study is obtained from the China Meteorological Agency (CMA). This dataset provides information on the center location, central pressure, and maximum wind speed of typhoon at 6-hour intervals (Ying et al., 2014; Lu et al., 2021).

2.3 Numerical Simulation

A high-resolution ocean model of Regional Ocean modeling System (ROMS) is developed to simulate the propagation of NIWs. TheROMS is a free surfaces, terrain-following model that solves nonlinear primitive equations on a staggered Arakawa C-grid (Shchepetkin and McWilliams, 2005).

The model domain spans 104°E~126°E and 8°N~25°N, using a horizontal resolution of 1/20°×1/20° (Figure 1). There are 40 layers in a stretched σ coordinate, with about 20 σ layers in the upper 300 m (Shchepetkin and McWilliams, 2005). The bathymetry is extracted from the General Bathymetric, Chart of the Oceans (GEBCO, Tozer et al., 2019). The initial and the open boundary conditions are derived from the climatological monthly mean Simple Ocean Data Assimilation (SODA, version 2.2.4, Carton and Giese, 2008). The model's atmospheric forcings, such as wind stress, net heat flux, and net fresh water flux are obtained from the Climate Forecast System Version 2 (CFSv2, Saha et al., 2014). The surface wind stress has a 0.203°×0.203° horizontal resolution and a hourly temporal resolution, while other forcing fields have a 0.5°×0.5° horizontal resolution and a 6-hour temporal resolution.

The model is integrated from a static status with a 6 s time step for the external mode, and a 120 s time step for the internal mode. The model conducts a hindcast run

from 1991 to 2011 after a 20-year climatology run for spin-up. After the hindcast run, the model conducts a typhoon forcing field simulation from 16 Aug. to 4 Nov., 2014.

3 Results

3.1 Model Evaluations

To validate the model results, the simulated profiles are compared with observations. Considering the completeness of observations, observed temperatures from Buoy-4 and observed ocean currents from Buoy-1 are showed (Figures 2 and 3). The temperatures under the influence of a typhoon are a crucial indicator of the air-sea interaction. Therefore, the sea temperature anomalies following the passage of Typhoon Kalmaegi are computed to evaluate the model results (Figure 2).

Typhoon Kalmaegi was closest to Buoy-4 at about 00:00 UTC on Sep. 15, 2014. Typhoon Kalmaegi causes a discernible reduction in sea surface temperature (SST), and the data obtained from Buoy-4 and model outputs demonstrate similar magnitudes of SST drops (Figures 2b and 2d). Furthermore, following the passage of the typhoon, the temperature of the mixed layer decreases, and the temperature of the thermocline increases, accompanied by changes of the sea temperature structure (Figures 2a and 2c). Although the model results show a deeper thermocline compared to the *in-situ* data, considering the coarse resolution of the in-situ data and the model bias, the differences are acceptable.

Figure 3 shows the wind speeds from the Buoy-2 and CFSv2, as well as the observed ocean currents. Generally speaking, the wind speed provided by the CFSv2 is in good agreement with the observations, and the structure of the ocean current simulated by ROMS is also consistent with the observations.

The near-inertial current velocity is obtained by a 4^{th}-order Butterworth bandpass filter. The cut-off frequencies are [0.9-1.1]*f*. In response to the Typhoon Kalmaegi, the near-inertial current velocity in the mixed layer begin to intensify at around 12:00 UTC on Sep. 13, 2014. Subsequently, it gradually weakens and spreads to the thermocline and subsurface at about 18:00 UTC on Sep. 20, 2014. The strength of the near-inertial current velocity in the thermocline is weaker than that in the mixed layer

(Figures 4a and 4c). In comparison with the near-inertial current velocity observed by Buoy-2, the model results show a similar pattern, with the bias of current velocities is acceptable (Figures 4b and 4d). These relatively small differences between the observations and the model results indicate that the model results are reliable for studying the generation, propagation, and dissipation of the NIWs caused by Typhoon Kalmaegi.

3.2 Dynamics on Different Sides of the Typhoon Track

To analyze the NIE transported to the ocean interior from Typhoon Kalmaegi, the NIE is calculated using the following formula,

$$NIE = \frac{1}{2}\rho_0(u_i^2 + v_i^2)$$

where $\rho_0 = 1025$ kg/m^3 is the reference density of seawater, u_i and v_i are the zonal and meridional near-inertial velocities obtained by the bandpass filter, respectively.

Figures 5 and 6 show the vertical profiles of the NIE at selected stations on both sides of Typhoon Kalmaegi's track. Both the depth of the mixed layer and the depth of pycnocline are overlaid. The depth of the mixed layer is defined using the threshold method with a finite difference criterion (de Boyer Montégut et al., 2004). Firstly, the density increment is calculated as follows,

$$\Delta\rho = |\rho(T_z - \Delta T, S_z, P_0) - \rho(T_z, S_z, P_0)|$$

where T_z is the temperature at the reference depth, which is set at 10m depth, ΔT is taken as 0.5℃, S_z is taken as 35.0, and $P_0 = 0$ is the sea surface pressure. The depth of the mixed layer is defined as the depth where the density is greater than the reference density (density value at 10m depth) by $\Delta\rho$. The bottom of the pycnocline is defined based on gradient threshold criterion, i.e., the depth where vertical density gradient is greater than 0.02 kg/m^3 is deemed the bottom of pycnocline.

As shown in Figures 5, and 6, NIE in the mixed layer increases rapidly due to strong wind stress, when Typhoon Kalmaegi passed the ocean surface. Additionally, at stations to the right side of the typhoon track (Figures 5a and 6a), NIE in the upper

ocean is stronger than that to the left side (Figures 5b and 6b), which is consistent with previous studies (Chang and Anthes 1978). . However, NIE below the mixed layer on the left side of the typhoon track is equally strong as that on the right side of the typhoon track. Such feature is evident in Figure 5b, where the NIE in the deep ocean at station L1 is stronger than that at station R1 (yellow triangles in Figure 1) . A similar pattern is also observed in Figure 6b.

The NIE injection into deep ocean shows different characteristics on both sides of typhoon track. The different changes in ocean stratification on both sides of typhoon, which influence the propagation of inertial internal waves into the deep sea, play a vital role in the transport of NIE. On both sides of the typhoon, the combined action of “heat pumping” and “cold suction” causes different changes in ocean stratification. Taking stations R1 and L1 as an example, the wind speeds on the right side of the typhoon track are faster, causing stronger mixing and entrainment effects, and the uplift caused by suction is weaker. Therefore, “heat pumping” dominates both the mixed layer and pycnocline. The mixed layer and pycnocline of station R1 deepens rapidly at the same time (Figure 5a). On the left side of the typhoon track, at station L1, slower wind speed lead to weaker mixing and entrainment effects compare with the right side. As a result, while “heat pumping” still dominates the mixed layer, “cold suction” plays a more important role in the pycnocline (Figure 5b). The different proportions of the two effects at different layers cause the deepening of the mixing layer and the lifting of the pycnocline at station L1, thus result in stronger compression of the pycnocline. This compression is a trigger of NIWs (Ding et al., 2018), which makes NIE of station L1 stronger than that of station R1 in the subsurface. However, station R1 is located near the center of the track of the subsequent Typhoon Fung-Wong, so the pycnocline of station R1 is significantly uplifted again after about September 20, 2014. While station L1 is far away from Typhoon Fung-Wong, so it is slightly affected. Stations R2 and L2 exhibit similar properties, but due to changes in typhoon intensity and direction, they are not as discernible as stations R1 and L1. The reasons for this will be further explained below through the distribution of sea surface vorticity.

Figure 7 shows the vorticity distributions around stations R1 and L1 (a-d) as well as stations R2 and L2 (e-h) before and after passage of Typhoon Kalmaegi. The positive vorticity near station L1 is significantly higher than that around station R1 when Typhoon Kalmaegi is closest to stations R1 and L1 (Figure 7b). This finding confirms that the "cold suction" on the left side of the typhoon track plays a more important role. This suction, together with the mixing and entrainment caused by Typhoon Kalmaegi in the mixed layer, lead to a stronger compression of the pycnocline, which drives stronger NIWs on the left side of the typhoon track. However, after Typhoon Kalmaegi's passage, there is no noticeable difference in vorticity distribution on both sides of the typhoon track. Therefore, the propagation of NIWs will not be hindered by the positive vorticity (Lee and Niiler, 1998; Zhang et al., 2015; Zhang et al., 2019; Yang et al., 2021). A similar phenomenon is observed in Figures7e-7h. Still, the positive vorticity near station L2 is not stronger than that of station R2 due to the turn of Typhoon Kalmaegi as it went by the stations. This turn makes the difference of the NIE in the deep ocean between stations R2 and L2 not as significant as that between stations R1 and L1.

3.3 Effects of Stratification Changes on Vertical Propagation of NIE

To further analyze the changes in stratification and energy caused by Typhoon Kalmaegi, the potential density, buoyancy frequency, and rotary spectra of velocity at the selected stations are calculated (Figure 8). Rotary spectral analysis allows for diagnosing changes in horizontal velocity rotation direction with respect to time or depth (Leaman and Sanford, 1975). In this section, the rotary frequency spectra are used to analyze the energy changes at each depth and frequency band, and the rotary wavenumber spectra are used to determine the vertical propagation direction of energy.

The current velocity time series before (UTC 00:00 on Aug.15, 2014 – UTC 08:00 on Sep.16, 2014) and after (UTC 04:00 on Sept.12, 2014 – UTC 12:00 on Oct.14, 2014) Typhoon Kalmaegi's arrival at each station are selected for the rotary

frequency spectrum analysis. The clockwise spectra and counter clockwise spectra are combined to obtain the total spectra. The total spectra are scaled as

$$S_{std} = \log_{10} \frac{S}{1 \times 10^{-8}}$$

where S is the original spectra, and S_{std} is the scaled spectra.

Significant spectral density peaks around diurnal and semidiurnal tide frequencies are observed over the entire depth before the passage of Typhoon Kalmaegi (Figure 8). Although there is strong spectral density near the near-inertial frequency, it is not solely concentrated in that frequency, but distributes across the whole low-frequency band. It is mainly distributes above the depth of 400 m. After the Typhoon Kalmaegi's passage, the spectral density of each frequency band enhances to varying degrees and is mainly concentrated in the near-inertial frequency above the depth of 800 m. The distribution of spectral density peaks around the near-inertial frequency gradually broadens with depth. A discontinuity is observed near the bottom of the pycnocline due to the strongest stratification. It is noticed that since the stronger wind stress on the right side of the typhoon track induces stronger near-inertial current velocities on the ocean surface, spectral density of the mixed layer and upper pycnocline at stations R1 and R2 is more elevated than that at stations L1 and L2 in the near-inertial frequency. However, below the pycnocline, the spectral density of the near-inertial frequency at stations L1 and L2 is stronger than that at stations R1 and R2, and it is more prominent below the depth of 300 m (black boxes in Figure 8). This indicates that the vertical propagation of the NIE to the deep ocean at stations L1 and L2 is more significant.

As explained in Section 3.2, these differences are related to the changes in oceanic stratification. Figure 8 shows the vertical profiles of buoyancy frequency, there is no discernible change in buoyancy frequency at stations R1 and R2 after Typhoon Kalmaegi's passage. However, at stations L1 and L2, the buoyancy frequency increases significantly due to the deepening of the mixed layer and the uplifting of the pycnocline after the passage of Typhoon Kalmaegi, indicating that the pycnocline and oceanic stratification become stronger. Higher buoyancy frequency

represents a more stable stratification, which is necessary condition for the propagation of NIWs (Cuypers et al., 2013). The propagation of NIE to the deep ocean is mainly occurs through the NIWs, which can propagate in three dimensions (Lee and Niiler, 1998; Chen et al., 2013; Alford et al., 2016). The stronger stratification and the shallower depth of the stratification peak on the left side of the typhoon track are more conducive to the generation and propagation of NIWs (Alford, 2001). Previous studies and model results demonstrate that different oceanic stratification changes on the two sides of the typhoon track result in different injection of NIE by affecting the generation and propagation process of NIWs.

A rotary wavenumber spectrum is a useful method for determining the vertical energy propagation of NIWs. The clockwise spectra represent the downward propagation of energy, and the counter clockwise spectra represent the upward propagation of energy. For a more intuitive understanding of the difference in vertical energy propagation of NIWs on different sides of the typhoon track, the rotary wave number spectra of current velocities are shown in Figure 9. Before the passage of Typhoon Kalmaegi, the energy magnitudes of the clockwise spectra and the counter clockwise spectra are nearly the same. After the passage of Typhoon Kalmaegi, both the clockwise spectra and the counter clockwise spectra are enhanced to varying degrees and mainly concentrating in the clockwise spectra with a vertical wavelength greater than 200 m. The average clockwise spectra are over 5 times that of the counter clockwise spectra, indicating that the energy generated during the typhoon primarily propagated downward vertically. Compared with station R1, the energy of station L1 is more concentrated in the clockwise spectra (Figures 9a-9d). This indicates that at station L1, the energy is more concentrated in the down-transmitted part. Additionally, it is noticed that the spectral peaks of the clockwise spectra of station L1 are concentrated in the period of intense compression of the uplifted pycnocline and the deepened mixed layer after the passage of Typhoon Kalmaegi. This shows that the oceanic stratification changes caused by Typhoon Kalmaegi at station L1 are more conducive to the downward propagation of the NIE. A similar phenomenon exists at stations R2 and L2. Although the clockwise spectral values at station L2 are slightly

lower than those at station R2 in the first few days following the Typhoon Kalmaegi's passage, about 10 days later, the clockwise spectral values of station L2 exceeded those of station R2. Additionally, the clockwise spectral peaks on the right side of the typhoon track are often accompanied by the counter clockwise spectral peaks, which indicates that the downward propagation of the NIE on the right side of the typhoon track is not as significant as that on the left side.

Although the wind speed of typhoons greatly impacts the input of NIE, oceanic stratification dominates the propagation of NIWs and corresponding the transport of NIE. On the right side of the typhoon track, stronger wind stress excites stronger near-inertial current velocities at the ocean surface, and transport more mechanical energy to the ocean surface. However, stronger wind stress also results stronger mixing, which weakens oceanic stratification. Such condition is unfavorable to the generation and vertical propagation of NIWs. The average buoyancy frequency loss of 200 m over the ocean before (Aug. 29, 2014 - Sept. 13, 2014) and after (Sept. 13, 2014 - Sept. 28, 2014) the passage of Typhoon Kalmaegi also supports the conclusion (Figure 10).

As shown in Figure 10, the average buoyancy frequency loss of the upper surface on the right side of the typhoon track is significantly larger than that on the left side. This indicates that previous studies using the slab model or simply using the production of wind speed and near-inertial current velocities to analyze the input of NIE may underestimate the propagation of the NIE to the deep ocean on the left side of the typhoon track due to the neglect of changes in oceanic stratification caused by typhoons (Alford, 2003; Jiang et al., 2005).

3.4 Near-Inertial Energy Budget

To quantitatively analyze the propagation and transport of NIE during the typhoon, the NIE budget is calculated according to the following diagnosis equation (Zhai et al., 2009),

$$\frac{\partial}{\partial t}\int E_i\,dV = -\int (p_i\boldsymbol{u_i})\,dA_I + \int (\boldsymbol{\tau}\cdot\boldsymbol{u_i})\,dA_s - \int (\rho_i w_i g)dV - \int \left(\rho_0 K_V \left|\frac{\partial \boldsymbol{u_i}}{\partial z}\right|^2\right)dV + \int (others)\,dV$$

where subscript i indicates the near-inertial frequency band, E is the NIE, $(p_i \cdot \boldsymbol{u_i})$ is the NIE flux of three dimension, $(\boldsymbol{\tau}\cdot\boldsymbol{u_i})$ is the NIE input by wind at the sea surface, $(\rho_i w_i g)$ is the near-inertial potential energy, $(\rho_0 K_V \left|\frac{\partial \boldsymbol{u_i}}{\partial z}\right|^2)$ is the NIE sink caused by vertical viscous effects, $others$ is the remainder term, V is the control volume, A_I is the area of the side and bottom open boundaries of the control volume, and A_s is the sea surface area.

Furthermore, to determine the fraction of the NIE input by the typhoon to the total mechanical energy, the total mechanical energy transported to the ocean during the typhoon is estimated by the following equation (Nam et al., 2012),

$$\int (\boldsymbol{\tau}\cdot\boldsymbol{u})\,dA_s$$

where $\boldsymbol{\tau}$ is the wind stress, $\boldsymbol{u}$ is the current velocity.

Table 1. The NIE budget for the top 300 m of the region is enclosed by the box shown in Fig.1 and integrated for the 13-day, and 20-day intervals. A_B represents the area of the bottom open boundary, A_M represents the meridional boundaries of the area, and A_Z represents the zonal boundaries of the area. The number in parentheses is the ratio of each energy term to the wind NIE input.

Terms of NIE Budget Equation		Energy/J （Ration of each energy term to the wind NIE input）	
		UTC 0600 on September 13- UTC 0000 on September 26	UTC 0600 on September 13- UTC 0600 on October 3
Wind NIE input	$\int (\boldsymbol{\tau}\cdot\boldsymbol{u_i})\,\mathrm{d}A_s$	6.0×10^{15}	6.1×10^{15}
Viscous removal in the top 300 m	$\int \left(\rho_0 K_V \left\|\frac{\partial \boldsymbol{u_i}}{\partial z}\right\|^2\right)\mathrm{d}V$	2.3×10^{15} (38.0%)	2.4×10^{15}(40.0%)
Conversion to inertial potential energy	$\int (\rho_i w_i g)dV$	6.5×10^{13} (1.07%)	3.5×10^{13}(0.57%)
Zonal NIE flux through the boundary	$\int (p_i u_i)\,\mathrm{d}A_Z$	1.4×10^{14} (2.20%)	1.8×10^{14}(3.0%)
Meridional NIE flux	$\int (p_i v_i)\,\mathrm{d}A_M$	9.8×10^{12} (0.16%)	7.0×10^{12}(0.12%)

through the boundary			
Vertical NIE flux at the depth of 300m	$\int (p_i w_i)\, \mathrm{d}A_B$	2.6×10^{15} (43.5%)	3.1×10^{15}(51.6%)

In this study, the NIE budget for the upper 300 m of the region defined by the box shown in Figure 1 is calculated and integrated for the periods of 13-day, and 20-day, respectively. The total mechanical energy input from Typhoon Kalmaegi is estimated to be about 4.1×10^{16} J, with approximately 15% of this energy being injected into the near-inertial frequency band. The energy injection into the upper ocean on the right side of the typhoon track is typically stronger (Figure 11), which is consistent with the previous studies (Price, 1981, 1983; Zhang et al., 2016). About 32% of the NIE is dissipated in the mixed layer, while about 40% of the NIE is dissipated in the upper 300 m of the ocean due to turbulent mixing. The high energy dissipation corresponds with the high NIE input, and occurred within a short period after the passage of Typhoon. The turbulent mixing not only dissipates energy but also weakens the stratification. As a result, variations in dissipation and stratification changes results in the inconsistent distribution of NIE input at the sea surface and propagate to the deep sea. The 3D NIE flux will be used to demonstrate the conclusion.

The calculating NIE budget shows that more than 50% of the NIE remained and propagated in the local area for more than 20 days after Typhoon Kalmaegi left the area. As Figures 12a and 12b demonstrate, strong horizontal NIE fluxes are distributed near the typhoon track, and there is no discernible difference between both sides of the typhoon track. Regarding the vertical propagation of NIE, as Table 1 shows, within 13 days after the passage of Typhoon Kalmaegi, NIE propagated downward through the depth of 300 m was 2.6×10^{15} J, accounting for 43.5% of the total NIE input. This proportion increased to 50% within 20 days after the passage of Typhoon Kalmaegi. This ratio is higher than results of Zhai et al. (2009), in which the NIE transport into the deep ocean is only 10% under the general climate condition. This indicates that the NIE input by typhoons may penetrate to the deep ocean more easily. The left side of the typhoon track has a discernible downward vertical NIE

fluxes, which corresponds well to the small values of buoyancy frequency loss (Figure 10 and 12c). This phenomenon may be affected by the southward NIE flux, but there is almost the same magnitude of southward NIE flux in the area of elevated vertical NIE flux, so the influence of this factor can be excluded. The results demonstrate that despite the sea surface input of NIE being higher on the right side of the typhoon track, the injection of inertial energy transport to the deep ocean is stronger on the left side. This is attributed to differing turbulent dissipation and stratification responses on both sides of the typhoon track.

4 Conclusion and Discussion

In deeper water, the so-called “inertial pumping” mechanism excites NIWs, i.e., temporal fluctuation wind stress produces inertial currents in the surface mixed layer. If inertial currents are horizontally divergent, the vertically fluctuating base of the mixed layer “pumps” NIWs in the stratified ocean interior (Price, 1983). The vertical propagation of NIWs from the mixed layer into the thermocline is a crucial ingredient in current conceptions of how the upper ocean is mixed. The vertical propagation of NIWs depends on the vertical group velocity, i.e., $C_g \approx -N^2 k_h^2 / 2 f k_z^3$ Previous studies focus on β-effect and mesoscale vorticity field, which leads to a systematic reduction of the horizontal scale of near-inertial waves (D’Asaro et al., 1995; Kunze, 1985; Asselin and Young, 2020). Ocean stratification (N) and horizontal wavenumber play equivalent role according to the group velocity.

Determining how "heat pumping" and "cold suction" of typhoons impact ocean stratification is crucial to understand the generation, propagation, and dissipation mechanisms of NIWs under typhoons. In this study, the ROMS is used to simulate the NIWs generated by Typhoon Kalmaegi. The results show that the different responses in ocean stratification significantly influence the generation and propagation of NIWs. On the right side of the typhoon track, the “heat pumping” caused by the strong wind stress dominates the mixed layer and the upper pycnocline. The turbulent mixing caused by the stronger “heat pumping” on the right side of the typhoon track, not only

dissipates more energy but also weakens the stratification strength. On the left side, the "heat pumping" dominates the mixed layer, while the "cold suction" dominates the pycnocline and deep ocean, creating more favorable stratification changes and stronger compression in the pycnocline. The stronger compression of the mixed layer and the pycnocline, along with more favorable stratification condition, result in stronger NIWs and stronger downward propagation of NIE on the left side of the typhoon track. As a result, although the wind energy input at the sea surface is much higher on the right side of the typhoon track, the injection of inertial energy transport to the deep ocean is stronger on the left side.

By analyzing the effect of the "heat pumping" and "cold suction", we have attempted to improve understanding of the generation, propagation, and dissipation mechanisms of NIWs from an aspect of stratification. Our study also suggests that the NIE input by typhoons may penetrate to the deep ocean more easily, which means the contribution of typhoons to diapycnal mixing may have been underestimated in the present numerical model. Since climate models cannot yet directly simulate typhoons, our work can provide a new perspective on how to design a proper parameterization scheme to account for typhoon effects in climate models.

Acknowledgements

This study was supported by the National Nature Science Foundation of China (Grant No.42076015). The modeling work was performed on TianHe-1(A) at National Supercomputer Center in Tianjin.

Open Research

The observed and simulated data were deposited on Zenodo and available online (https://zenodo.org/record/8186605, Qian et al., 2023). The topography data were provided by General Bathymetric, Chart of the Oceans (https://www.gebco.net/data_and_products/gridded_bathymetry_data/), The initial and boundary condition data is derived from Simple Ocean Data Assimilation 2.2.4

(http://sodaserver.tamu.edu/assim/SODA_2.2.4/). The forcing data is derived from Climate Forecast System Version 2 (http://rda.ucar.edu/datasets/ds094.0/).The typhoon data derived from China Meteorological Agency (http://tcdata.typhoon.org.cn). Figures were made with Matlab version 9.12.0.1884302 (R2022a), available under the Matlab license at https://www.mathworks.com/products/matlab.html (Matlab, 2022).

Reference

Alford, M.H., 2003. Improved global maps and 54-year history of wind-work on ocean inertial motions. Geophysical Research Letters 30. https://doi.org/10.1029/2002GL016614

Alford, M.H., 2001. Internal Swell Generation: The Spatial Distribution of Energy Flux from the Wind to Mixed Layer Near-Inertial Motions. Journal of Physical Oceanography 31, 2359–2368. https://doi.org/10.1175/1520-0485(2001)031<2359:ISGTSD>2.0.CO;2

Alford, M.H., MacKinnon, J.A., Simmons, H.L., Nash, J.D., 2016. Near-Inertial Internal Gravity Waves in the Ocean. Annual Review of Marine Science 8, 95–123. https://doi.org/10.1146/annurev-marine-010814-015746

Asselin, O., Young, W.R., 2020. Penetration of Wind-Generated Near-Inertial Waves into a Turbulent Ocean. Journal of Physical Oceanography 50, 1699–1716. https://doi.org/10.1175/JPO-D-19-0319.1

Carton, J.A., Giese, B.S., 2008. A Reanalysis of Ocean Climate Using Simple Ocean Data Assimilation (SODA). Monthly Weather Review 136, 2999–3017. https://doi.org/10.1175/2007MWR1978.1

Chang, S.W., Anthes, R.A., 1978. Numerical Simulations of the Ocean's Nonlinear, Baroclinic Response to Translating hurricanes. Journal of Physical Oceanography 8, 468–480. https://doi.org/10.1175/1520-0485(1978)008<0468:NSOTON>2.0.CO;2

Chen, D., Lei, X., Wang, W., Wang, G., Han, G., Zhou, L., 2013. Upper Ocean Response and Feedback Mechanisms to Typhoon. Advances in Earth Science 28, 1077. https://doi.org/10.11867/j.issn.1001-8166.2013.10.1077

Chen, G., Xue, H., Wang, D., Xie, Q., 2013. Observed near-inertial kinetic energy in the northwestern South China Sea. Journal of Geophysical Research: Oceans 118, 4965–4977. https://doi.org/10.1002/jgrc.20371

Cuypers, Y., Le Vaillant, X., Bouruet-Aubertot, P., Vialard, J., McPhaden, M.J., 2013. Tropical storm-induced near-inertial internal waves during the Cirene experiment: Energy fluxes and impact on vertical mixing. Journal of Geophysical Research: Oceans 118, 358–380. https://doi.org/10.1029/2012JC007881

D'asaro, E.A., 1995. Upper-Ocean Inertial Currents Forced by a Strong Storm. Part III: Interaction of Inertial Currents and Mesoscale Eddies. Journal of Physical

Oceanography 25, 2953–2958. https://doi.org/10.1175/1520-0485(1995)025<2953:UOICFB>2.0.CO;2
de Boyer Montégut, C., Madec, G., Fischer, A.S., Lazar, A., Iudicone, D., 2004. Mixed layer depth over the global ocean: An examination of profile data and a profile-based climatology. Journal of Geophysical Research: Oceans 109. https://doi.org/10.1029/2004JC002378
Ding, W., Liang, C., Liao, G., Li, J., Lin, F., Jin, W., Zhu, L., 2018. Propagation characteristics of near-inertial waves along the continental shelf in the wake of the 2008 Typhoon Hagupit in the northern South China Sea. Bulletin of Marine Science 94, 1293–1311. https://doi.org/10.5343/bms.2017.1036
Emanuel, K., 2001. Contribution of tropical cyclones to meridional heat transport by the oceans. Journal of Geophysical Research: Atmospheres 106, 14771–14781. https://doi.org/10.1029/2000JD900641
Emanuel, K.A., 1986. An Air-Sea Interaction Theory for Tropical Cyclones. Part I: Steady-State Maintenance. Journal of the Atmospheric Sciences 43, 585–605. https://doi.org/10.1175/1520-0469(1986)043<0585:AASITF>2.0.CO;2
Ferrari, R., Wunsch, C., 2009. Ocean Circulation Kinetic Energy: Reservoirs, Sources, and Sinks. Annual Review of Fluid Mechanics 41, 253–282. https://doi.org/10.1146/annurev.fluid.40.111406.102139
Furuichi, N., Hibiya, T., Niwa, Y., 2008. Model-predicted distribution of wind-induced internal wave energy in the world's oceans. Journal of Geophysical Research: Oceans 113. https://doi.org/10.1029/2008JC004768
Gill, A.E., 1984. On the Behavior of Internal Waves in the Wakes of Storms. Journal of Physical Oceanography 14, 1129–1151. https://doi.org/10.1175/1520-0485(1984)014<1129:OTBOIW>2.0.CO;2
Hou, H., Xu, T., Li, B., Yang, B., Wei, Z., Yu, F., 2022. Different Types of Near-Inertial Internal Waves Observed by Lander in the Intermediate-Deep Layers of the South China Sea and Their Generation Mechanisms. Journal of Marine Science and Engineering 10, 594. https://doi.org/10.3390/jmse10050594
Jacob, S.D., Shay, L.K., Mariano, A.J., Black, P.G., 2000. The 3D Oceanic Mixed Layer Response to Hurricane Gilbert. Journal of Physical Oceanography 30, 1407–1429. https://doi.org/10.1175/1520-0485(2000)030<1407:TOMLRT>2.0.CO;2
Jiang, J., Lu, Y., Perrie, W., 2005. Estimating the energy flux from the wind to ocean inertial motions: The sensitivity to surface wind fields. Geophysical Research Letters 32. https://doi.org/10.1029/2005GL023289
Korty, R.L., Emanuel, K.A., Scott, J.R., 2008. Tropical Cyclone–Induced Upper-Ocean Mixing and Climate: Application to Equable Climates. Journal of Climate 21, 638–654. https://doi.org/10.1175/2007JCLI1659.1
Kunze, E., 1985. Near-Inertial Wave Propagation In Geostrophic Shear. Journal of Physical Oceanography 15, 544–565. https://doi.org/10.1175/1520-0485(1985)015<0544:NIWPIG>2.0.CO;2

Leaman, K.D., Sanford, T.B., 1975. Vertical energy propagation of inertial waves: A vector spectral analysis of velocity profiles. Journal of Geophysical Research (1896-1977) 80, 1975–1978. https://doi.org/10.1029/JC080i015p01975

Lee, D.-K., Niiler, P.P., 1998. The inertial chimney: The near-inertial energy drainage from the ocean surface to the deep layer. Journal of Geophysical Research: Oceans 103, 7579–7591. https://doi.org/10.1029/97JC03200

Lu, X., Yu, H., Ying, M., Zhao, B., Zhang, S., Lin, L., Bai, L., Wan, R., 2021. Western North Pacific Tropical Cyclone Database Created by the China Meteorological Administration. Adv. Atmos. Sci. 38, 690–699. https://doi.org/10.1007/s00376-020-0211-7

Ma, Y., Wang, D., Shu, Y., Chen, J., He, Y., Xie, Q., 2022. Bottom-Reached Near-Inertial Waves Induced by the Tropical Cyclones, Conson and Mindulle, in the South China Sea. Journal of Geophysical Research: Oceans 127, e2021JC018162. https://doi.org/10.1029/2021JC018162

Munk, W., Wunsch, C., 1998. Abyssal recipes II: energetics of tidal and wind mixing. Deep Sea Research Part I: Oceanographic Research Papers 45, 1977–2010. https://doi.org/10.1016/S0967-0637(98)00070-3

Nam, S., Kim, D., Moon, W.M., 2012. Observed impact of mesoscale circulation on oceanic response to Typhoon Man-Yi (2007). Ocean Dynamics 62, 1–12. https://doi.org/10.1007/s10236-011-0490-8

Park, J.J., Kwon, Y.-O., Price, J.F., 2011. Argo array observation of ocean heat content changes induced by tropical cyclones in the north Pacific. Journal of Geophysical Research: Oceans 116. https://doi.org/10.1029/2011JC007165

Pasquero, C., Emanuel, K., 2008. Tropical Cyclones and Transient Upper-Ocean Warming. Journal of Climate 21, 149–162. https://doi.org/10.1175/2007JCLI1550.1

Pollard, R.T., 1980. Properties of Near-Surface Inertial Oscillations. Journal of Physical Oceanography 10, 385–398. https://doi.org/10.1175/1520-0485(1980)010<0385:PONSIO>2.0.CO;2

Pollard, R.T., 1970. On the generation by winds of inertial waves in the ocean. Deep Sea Research and Oceanographic Abstracts 17, 795–812. https://doi.org/10.1016/0011-7471(70)90042-2

Price, J.F., 1983. Internal Wave Wake of a Moving Storm. Part I. Scales, Energy Budget and Observations. Journal of Physical Oceanography 13, 949–965. https://doi.org/10.1175/1520-0485(1983)013<0949:IWWOAM>2.0.CO;2

Price, J.F., 1981. Upper Ocean Response to a Hurricane. Journal of Physical Oceanography 11, 153–175. https://doi.org/10.1175/1520-0485(1981)011<0153:UORTAH>2.0.CO;2

Price, J.F., Sanford, T.B., Forristall, G.Z., 1994. Forced Stage Response to a Moving Hurricane. Journal of Physical Oceanography 24, 233–260. https://doi.org/10.1175/1520-0485(1994)024<0233:FSRTAM>2.0.CO;2

Qian Z., Guanghong L., Feilong L., Weifang J., Chujin L., 2019. Analysis of upper ocean response to Typhoon Doksuri in the northwest South China Sea. hyxbzwb 41, 22–35. https://doi.org/10.3969/j.issn.0253-4193.2019.07.003

Saha, S., Moorthi, S., Wu, X., Wang, J., Nadiga, S., Tripp, P., Behringer, D., Hou, Y.-T., Chuang, H., Iredell, M., Ek, M., Meng, J., Yang, R., Mendez, M.P., Dool, H. van den, Zhang, Q., Wang, W., Chen, M., Becker, E., 2014. The NCEP Climate Forecast System Version 2. Journal of Climate 27, 2185–2208. https://doi.org/10.1175/JCLI-D-12-00823.1

Sanford, T.B., Price, J.F., Girton, J.B., 2011. Upper-Ocean Response to Hurricane Frances (2004) Observed by Profiling EM-APEX Floats. Journal of Physical Oceanography 41, 1041–1056. https://doi.org/10.1175/2010JPO4313.1

Shay, L.K., Chang, S.W., Elsberry, R.L., 1990. Free Surface Effects on the Near-Inertial Ocean Current Response to a Hurricane. Journal of Physical Oceanography 20, 1405–1424. https://doi.org/10.1175/1520-0485(1990)020<1405:FSEOTN>2.0.CO;2

Shay, L.K., Elsberry, R.L., 1987. Near-Inertial Ocean Current Response to Hurricane Frederic. Journal of Physical Oceanography 17, 1249–1269. https://doi.org/10.1175/1520-0485(1987)017<1249:NIOCRT>2.0.CO;2

Shchepetkin, A.F., McWilliams, J.C., 2005. The regional oceanic modeling system (ROMS): a split-explicit, free-surface, topography-following-coordinate oceanic model. Ocean Modelling 9, 347–404. https://doi.org/10.1016/j.ocemod.2004.08.002

Sriver, R.L., Huber, M., 2007. Observational evidence for an ocean heat pump induced by tropical cyclones. Nature 447, 577–580. https://doi.org/10.1038/nature05785

Tozer, B., Sandwell, D.T., Smith, W.H.F., Olson, C., Beale, J.R., Wessel, P., 2019. Global Bathymetry and Topography at 15 Arc Sec: SRTM15+. Earth and Space Science 6, 1847–1864. https://doi.org/10.1029/2019EA000658

Yang, B., Hu, P., Hou, Y., 2021. Observed Near-Inertial Waves in the Northern South China Sea. Remote Sensing 13, 3223. https://doi.org/10.3390/rs13163223

Ying, M., Zhang, W., Yu, H., Lu, X., Feng, J., Fan, Y., Zhu, Y., Chen, D., 2014. An Overview of the China Meteorological Administration Tropical Cyclone Database. Journal of Atmospheric and Oceanic Technology 31, 287–301. https://doi.org/10.1175/JTECH-D-12-00119.1

Young, W.R., Jelloul, M.B., 1997. Propagation of near-inertial oscillations through a geostrophic flow. Journal of marine research 55, 735–766.

Zhai, X., Greatbatch, R.J., Eden, C., Hibiya, T., 2009. On the Loss of Wind-Induced Near-Inertial Energy to Turbulent Mixing in the Upper Ocean. Journal of Physical Oceanography 39, 3040–3045. https://doi.org/10.1175/2009JPO4259.1

Zhang, H., Chen, D., Zhou, L., Liu, X., Ding, T., Zhou, B., 2016. Upper ocean response to typhoon Kalmaegi (2014). Journal of Geophysical Research: Oceans 121, 6520–6535. https://doi.org/10.1002/2016JC012064

Zhang, H., Wu, R., Chen, D., Liu, X., He, H., Tang, Y., Ke, D., Shen, Z., Li, J., Xie, J., Tian, D., Ming, J., Liu, F., Zhang, D., Zhang, W., 2018. Net Modulation of Upper Ocean Thermal Structure by Typhoon Kalmaegi (2014). Journal of Geophysical Research: Oceans 123, 7154–7171. https://doi.org/10.1029/2018JC014119

Zhang, Y., Liu, Z., Zhao, Y., Li, J., Liang, X., 2015. Effect of surface mesoscale eddies on deep-sea currents and mixing in the northeastern South China Sea. Deep Sea Research Part II: Topical Studies in Oceanography, The South China Sea Deep 122, 6–14. https://doi.org/10.1016/j.dsr2.2015.07.007

Zhou, L., Chen, D.K., Lei, X.T., Wang, W., Wang, G., Han, G., 2019. Progress and perspective on interactions between ocean and typhoon. Chinese Science Bulletin 64, 60–72.

Figures

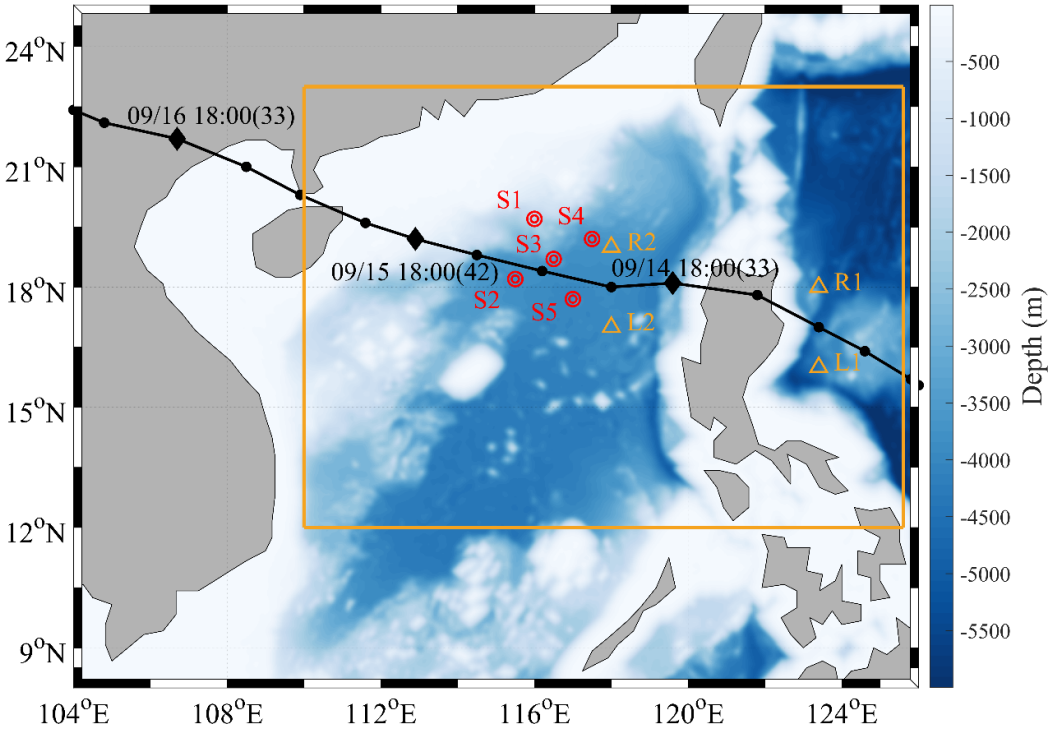

Figure 1. Numerical simulation domain and observation stations. The shaded color illustrates the SCS topography, and the yellow box is the analysis area in this study. The black line shows the track of Typhoon Kalmaegi between Sep.13-16 based on the best-track data from the CMA The maximum wind speeds (m/s) are denoted in brackets. The red circles indicate the locations of the buoy observation stations deployed in SCS, while the yellow triangles are selected analysis stations located on the different sides of the Typhoon Kalmaegi track.

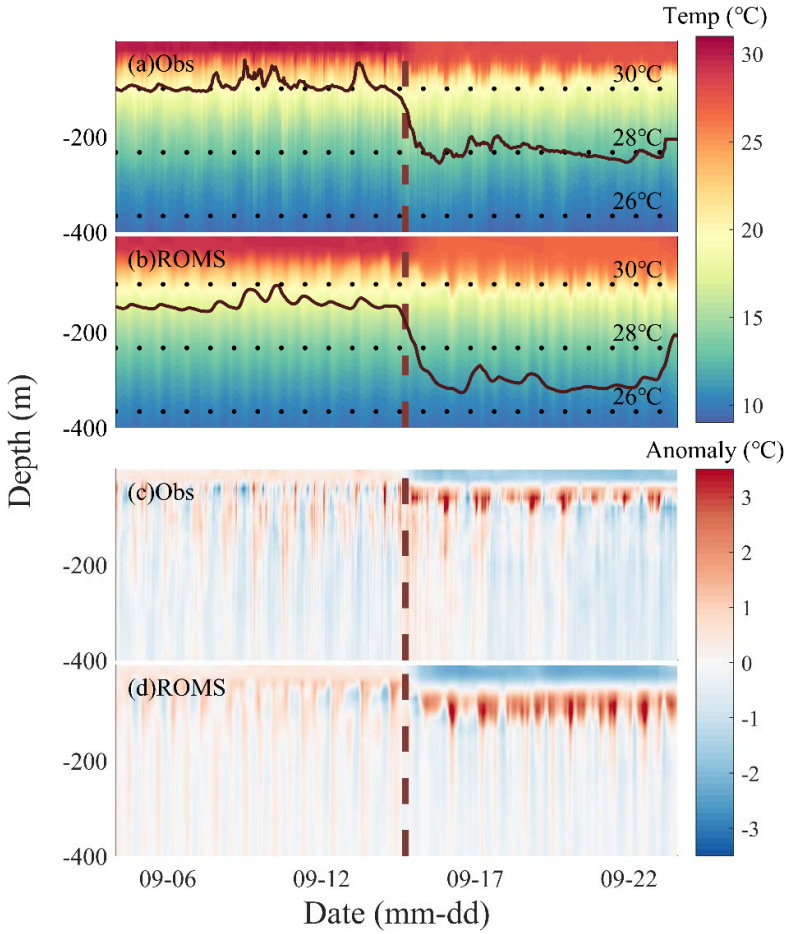

669

670 Figure 2. Comparison between observed and simulated temperature (a-b) and temperature
671 anomaly (c-d) at buoy-4 station. The black lines indicates SST time series 5m depth. The brown
672 dashed lines represent the time when Typhoon Kalmaegi was closest to buoy-4.

673

674

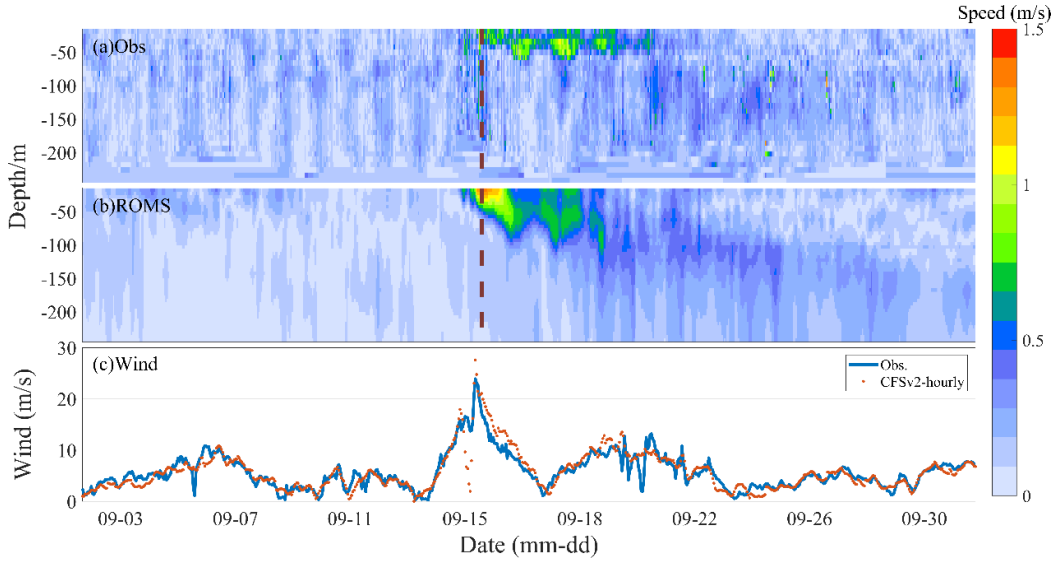

675

676 Figure 3. Comparison between observed and simulated ocean current (a-b) at buoy-2 station. The
677 brown dashed lines represent the time when Typhoon Kalmaegi was closest to the buoy-2. Wind
678 speed from the observations (buoy-2) and the CFSv2 data is shown in (c).

679

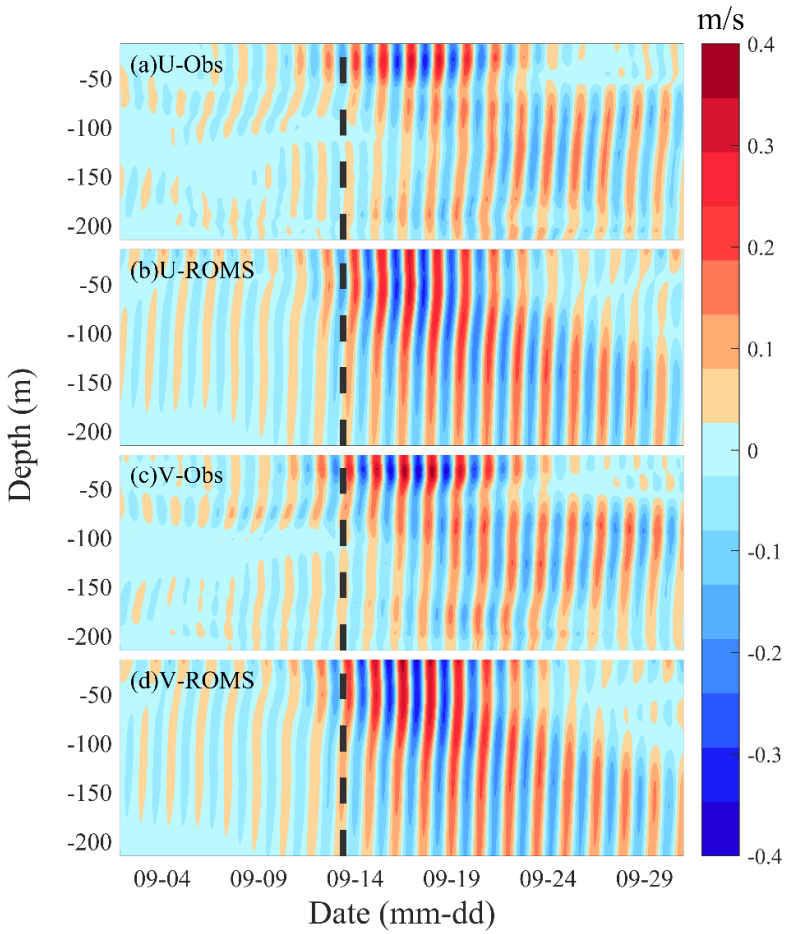

Figure 4. Comparison between observed and simulated near inertial current at buoy-2 station. Eastern component (a-b), northern component (c-d). The black dashed lines represent the time when Typhoon Kalmaegi was closest to buoy-2.

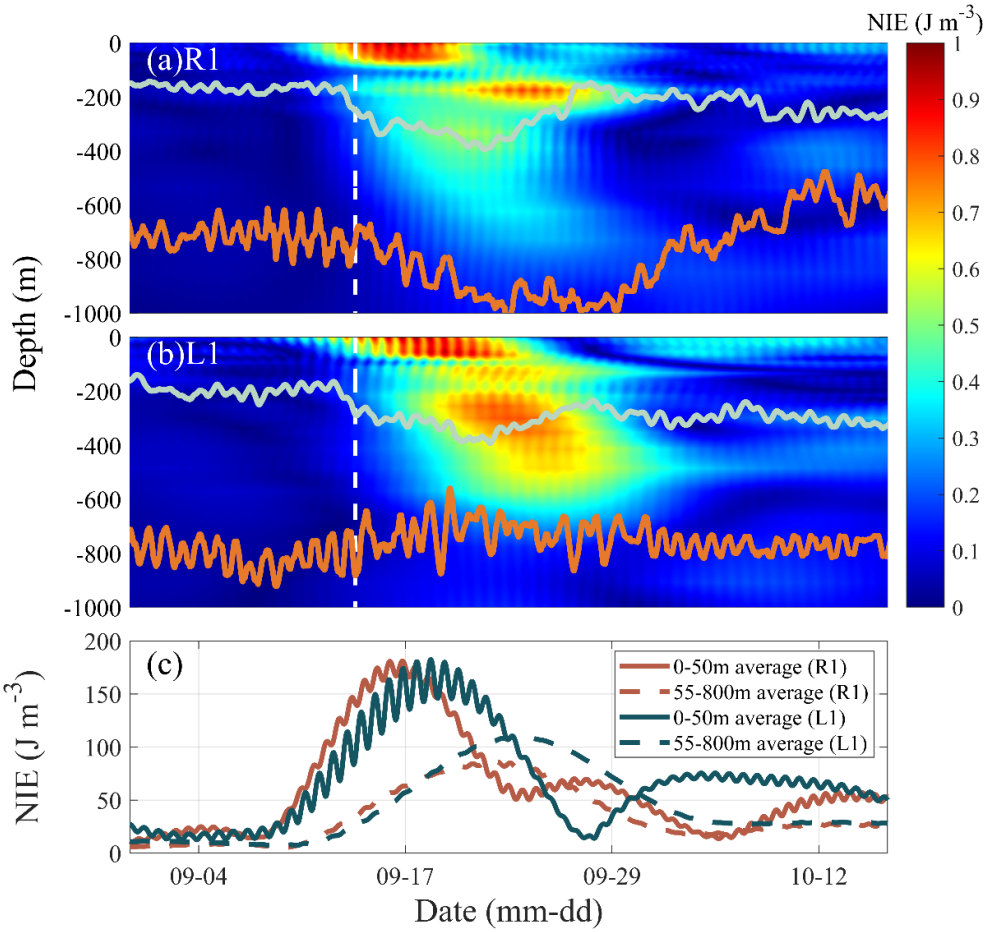

Figure 5 Vertical profiles of the NIE at station R1 and L1 (refer to Fig.1). The depth of the mixed layer (cyan lines) and the depth of pycnocline (orange lines) are overlaid. The white dashed lines represent the time when Typhoon Kalmaegi was closest to each analysis station. (c) show the averaged NIE of each station, with solid lines representing the 0-50m average value of NIE and dashed lines representing the 55-800m average value of NIE.

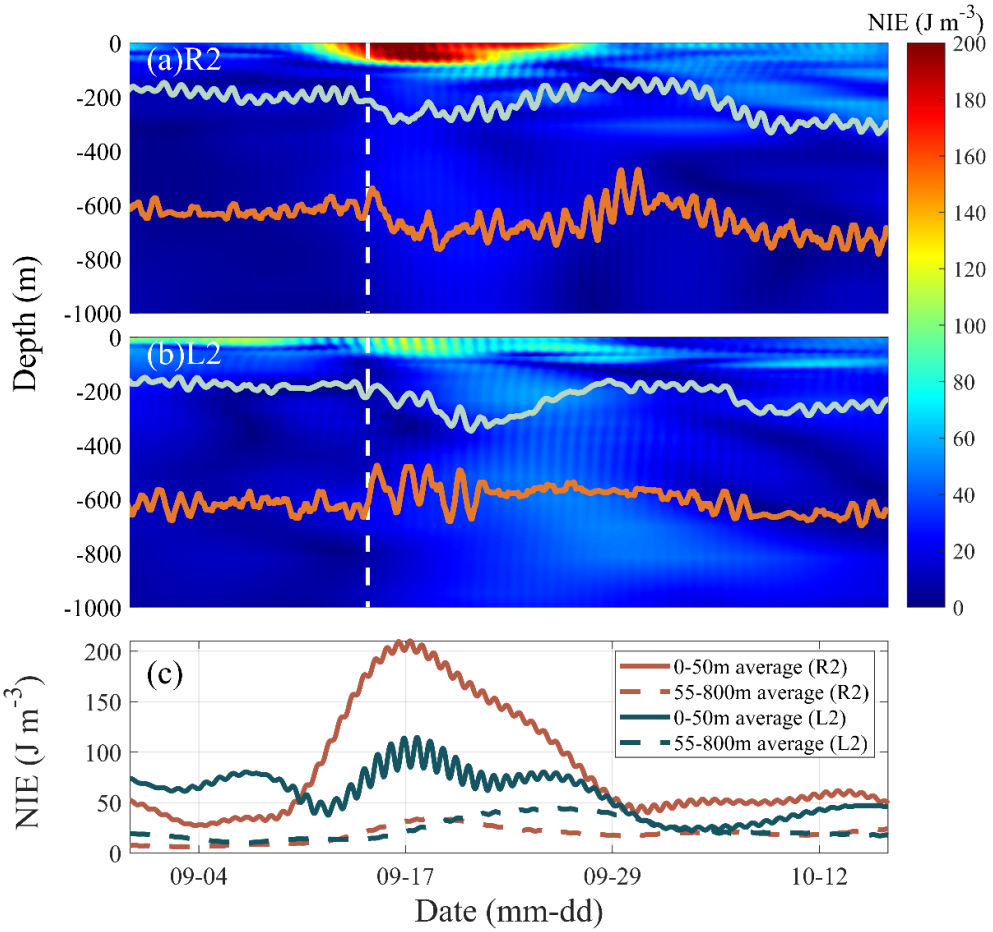

Figure 6 Vertical profiles of the NIE at station R2 and L2 (refer to Fig.1). The depth of the mixed layer (cyan lines) and the depth of pycnocline (orange lines) are overlaid. The white dashed lines represent the time when Typhoon Kalmaegi was closest to each analysis station. (c) show the averaged NIE of each analysis station, with solid lines representing the 0-50m average value of NIE and dashed lines representing the 55-800m average value of NIE.

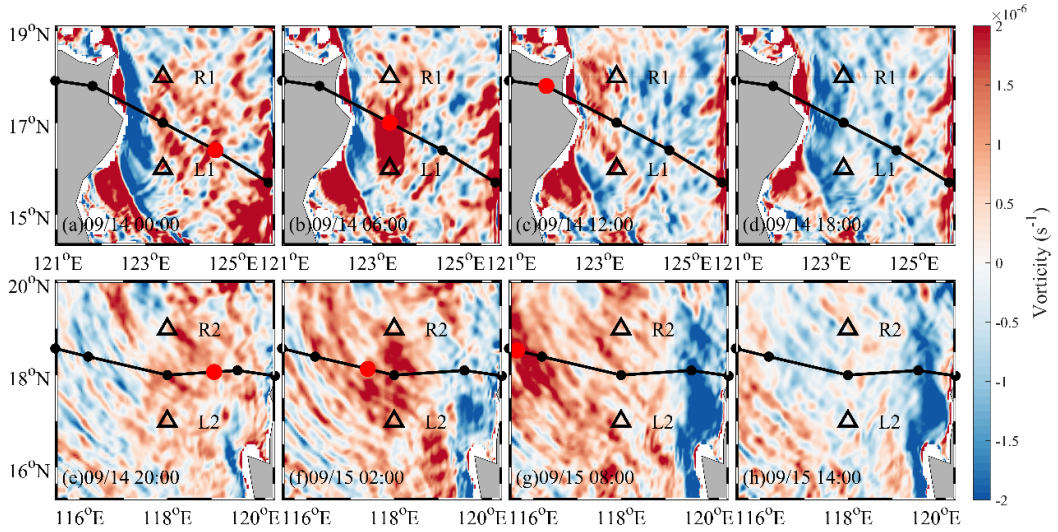

Figure 7. The vorticity distributions near stations R1 and L1 (a-d) and stations R2 and L2 (e-h) before and after passage of Typhoon Kalmaegi. The black lines denote the typhoon track, the red dot in each indicates the location of Typhoon Kalmaegi and the black triangles are locations used for analysis.

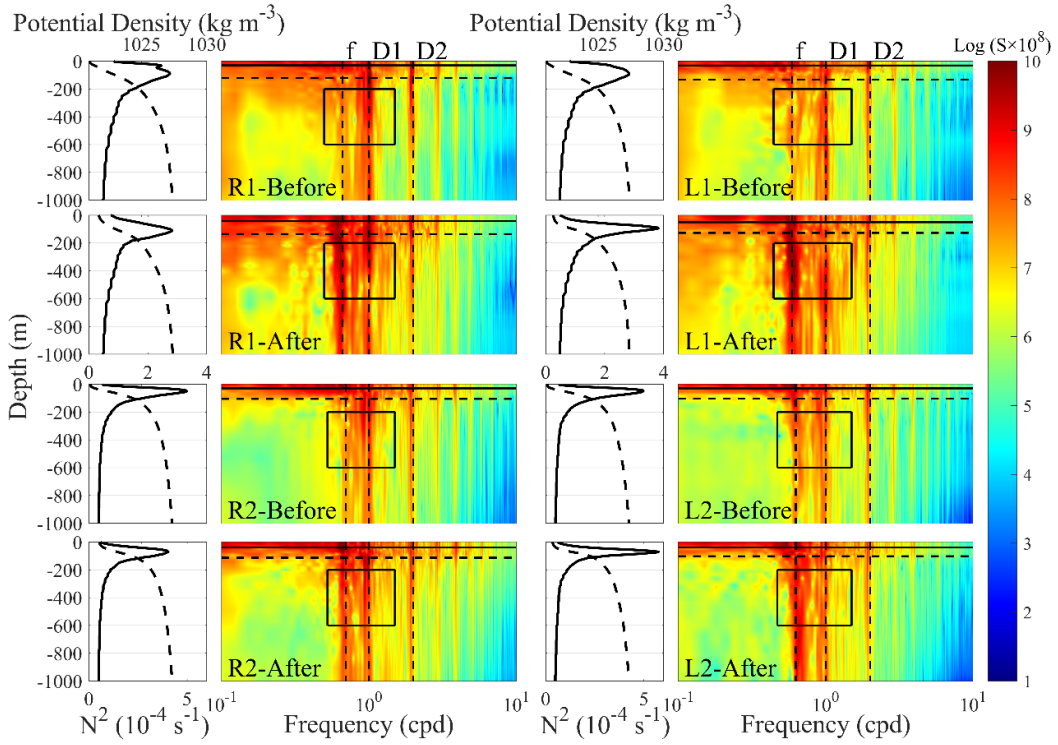

Figure 8. The potential density, buoyancy frequency, and spectra of the current velocities at each analysis station before and after the passage of Typhoon Kalmaegi. In the subgraphs with the white background, the solid lines represent the buoyancy frequency, corresponding to the lower x-axis, and the dashed lines represent the potential density, corresponding to the upper x-axis. The

717 shading color displays the processed spectra. The horizontal solid lines represent the average
718 depth of the mixed layer, the horizontal dashed lines represent the average depth of the pycnocline,
719 and the vertical dashed lines represent several typical frequency bands.

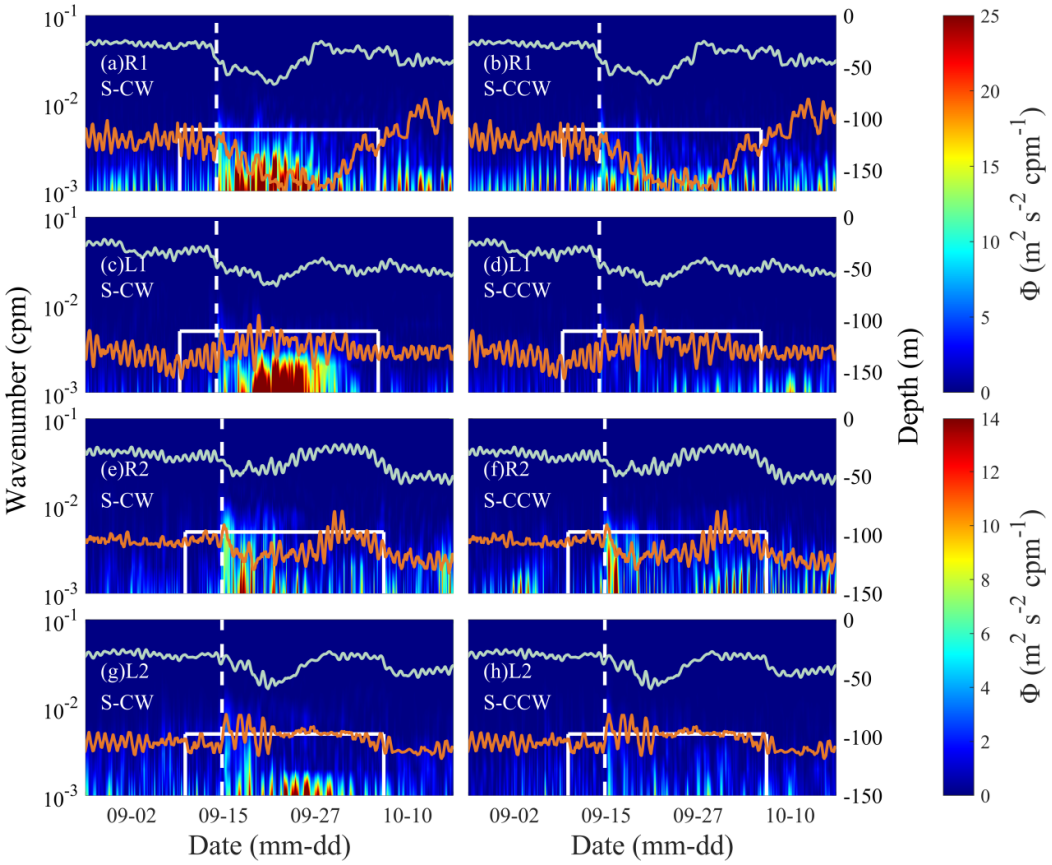

720

721 Figure 9. The rotary wavenumber spectra of the current velocities at four selected stations. The
722 cyan curves represent the depth of the mixed layer and the pycnocline averaged by the 12-hour
723 moving average, respectively. The white dashed lines indicates the times when Typhoon Kalmaegi
724 was nearest to each analysis station.

725

726

727

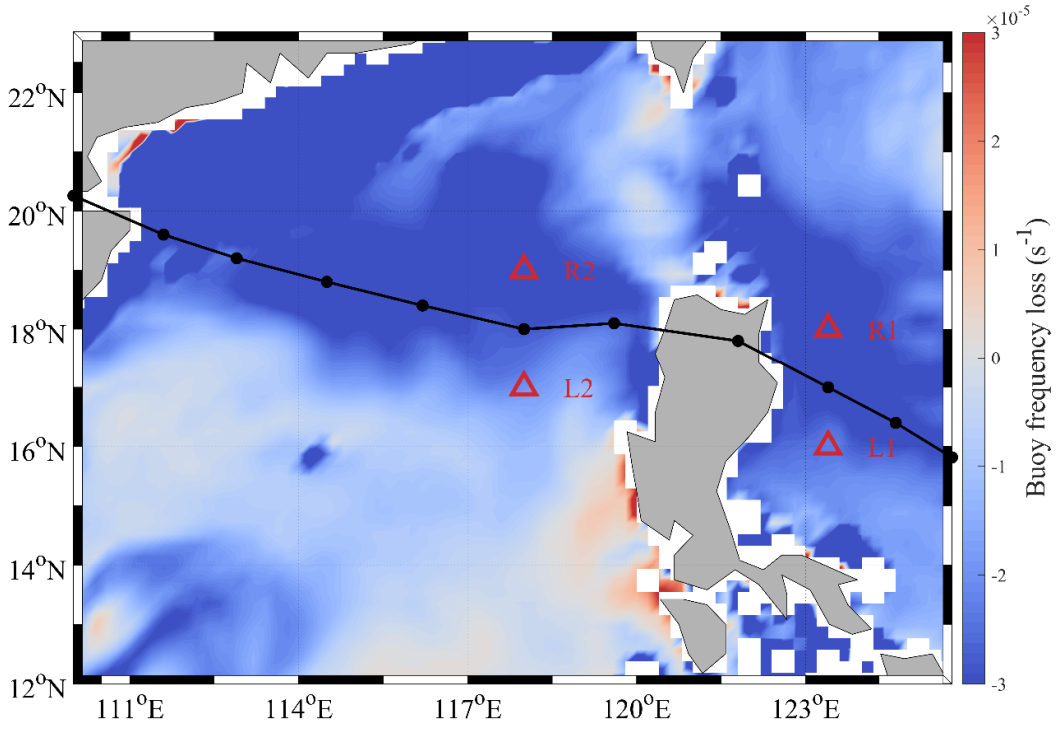

Figure 10. The average buoyancy frequency loss of 200m over the ocean before and after the passage of Typhoon Kalmaegi. The black curve is the typhoon track, and the red triangles are selected stations for analysis.

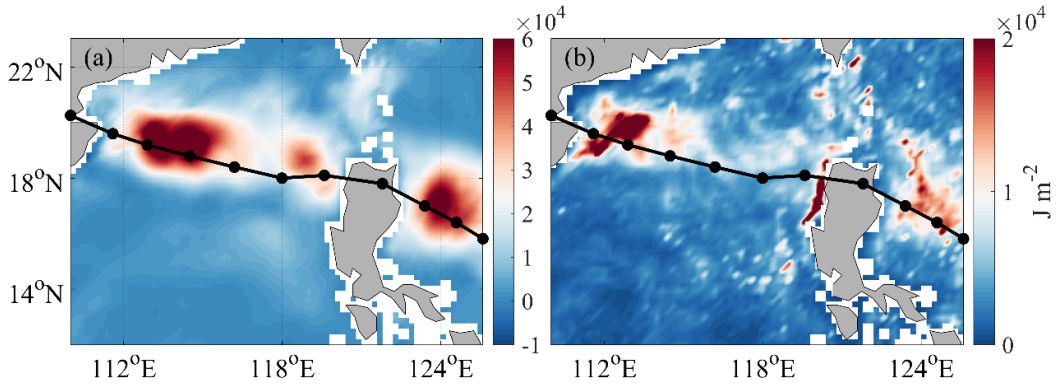

Figure 11. The NIE input by wind at the sea surface (a), and the NIE dissipated in the top 300m (b) integrated for the period of 20-days. The black curve is the typhoon track.

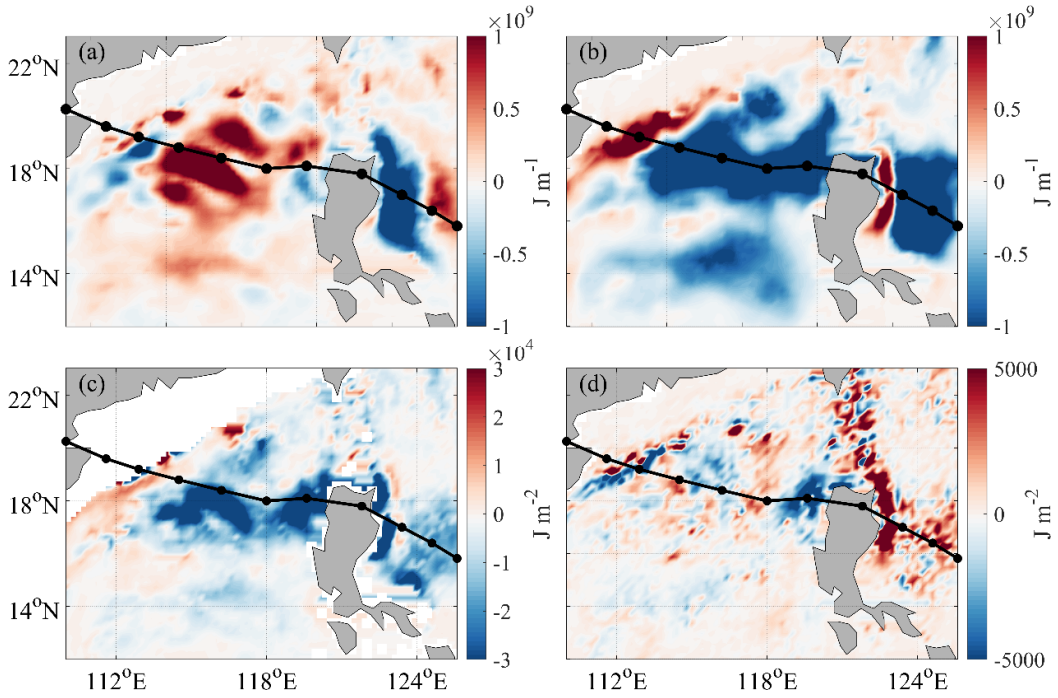

Figure 12. The zonal NIE flux (a), meridional NIE flux (b), Vertical NIE flux at the depth of 300m (c), and NIE that converts to inertial potential energy (d) integrated for the period of 20-days. The black curve is the typhoon track.